

Probing close-in satellites of Trans-Neptunian Objects through thermal and direct size measurements

J. M. Gómez-Limón¹, R. Leiva¹, J. L. Ortiz¹, P. Santos-Sanz¹, M. Kretlow^{2, 1}, Y. Kilic¹, J. L. Rizos¹,
A. Álvarez-Candal¹, and T. Müller³

¹ Instituto de Astrofísica de Andalucía, IAA-CSIC, Glorieta de la Astronomía s/n, 18008 Granada, Spain.

² Deutsches Zentrum für Astrophysik (DZA), Postplatz 1, 02826 Görlitz, Germany.

³ Max-Planck-Institut für extraterrestrische Physik, Giessenbachstr. 1, 85748 Garching, Germany.

Received dd mmm, 2026; accepted dd mmm, 2026

ABSTRACT

Context. Trans-Neptunian objects are distant bodies that retain valuable information about the origin and evolution of the Solar System. Many of these objects constitute binary systems. Studying binaries allows us to further characterise this primitive population and is critical for determining mass densities, a key but elusive physical property. Nevertheless, satellite detection can be challenging.

Aims. This study aims to constrain the presence of close-in satellites around a selection of ten trans-Neptunian objects, including four known binary systems used for methodology validation.

Methods. We developed a methodology independent of primary-secondary separation. We exploit the combination of occultation-derived sizes and thermal emission data from the "TNOs are Cool" *Herschel Space Observatory* key project. We model the thermal emission from a binary system to explain the thermal excess that cannot be reproduced by a single body of the occultation-derived size.

Results. We obtain satisfactory constraints for the validation targets (208996) Achlys, (229762) G!kún||'hòmdímà, (38628) Huya and (174567) Varda. We find that (84522) 2002 TC302, (119951) 2002 KX14, and (307261) Máni are likely binary systems, which was previously unknown. We report size estimates for their putative satellites. For (84922) 2003 VS2, (28978) Ixion, and (470316) 2007 OC10 we find that no sizable satellite is needed to reconcile thermal and occultation data.

Key words. Kuiper belt: general – Planets and satellites: detection – occultations

1. Introduction

Trans-Neptunian Objects (TNOs) populate the region of the Solar System beyond Neptune's orbit known as the Kuiper Belt. These objects are remnants of the planetesimal formation in the protoplanetary disk that gave birth to the planetary system we inhabit today, and they retain crucial information about its evolution (e.g. Nesvorný (2018); Fernández (2020); Gladman & Volk (2021)).

Trans-Neptunian Binaries (TNBs) are pairs of gravitationally bound TNOs. The Pluto/Charon system was the first binary system discovered in the Kuiper belt (Christy & Harrington 1978), although we now know it is a multiple system (Weaver et al. 2006, 2016). However, 35 years had to elapse for a second detection of a TNB to be confirmed (Veillet et al. 2002). Since then, many new TNBs have been discovered, accounting for a total of 144 as of February 2026¹. The study of TNBs has thrived in the last two decades, being one of the most active branches of Kuiper Belt research (e.g. Grundy et al. (2019b); Noll et al. (2020); Porter et al. (2024)).

One of the reasons for trying to detect binaries in the Kuiper Belt is that a characterisation of the mutual orbit constrains the system mass (Grundy et al. 2011; Parker et al. 2011; Grundy et al. 2019b). If independent size measurements are available, the density can be retrieved, informing us about bulk properties such

as ice-to-rock ratio or porosity. These properties are extremely difficult to attain otherwise.

The study of TNBs is also a pivotal method for testing the prediction of planetesimal formation theories and models. For example, the abundance of binary prograde orbits provides strong evidence in favour of the Streaming Instability (SI) (Nesvorný et al. 2019). This theory suggests that solid objects in the circumsolar disk began forming when small clusters of solid material created localised enhancements in gas drag, enabling these clusters to grow rapidly into full-sized TNOs (Youdin & Goodman 2005; Johansen et al. 2007; Bai & Stone 2010; Carrera et al. 2017).

The SI has grown to be the leading theory in planetesimal formation, and it is predicted to be very efficient in forming binary systems of roughly equal size (Nesvorný et al. 2010). This is consistent with observations suggesting that planetesimals formed almost entirely in binary pairs (Fraser et al. 2017). The chances are high that some of these primordial binary pairs survived their implantation in their current orbits, especially if they are tight systems (Nesvorný & Vokrouhlický 2019). In addition, Porter & Grundy (2012) performed Kozai Cycle Tidal Friction simulations, showing that TNBs orbits tend to shrink and circularise with time, leading to roughly ~30% of their randomised systems evolving into tight orbits with eccentricity $e < 10^{-4}$.

Other proposed mechanisms for binary system formation in the Kuiper Belt are giant collisions (Canup 2005), rotational fission (Ortiz et al. 2012) and grazing encounters (Leinhardt et al. 2010) or 'kiss-and-capture' scenarios (Denton et al. 2025). In

¹ See <https://www.johnstonsarchive.net/astro/asteroidmoons.html>

general, these mechanisms generate satellites around the parent bodies that might not be as equal-sized as those created by the SI. Most of the largest TNOs have moons. This is the case for 7 of the 8 largest TNOs (apart from Pluto): Eris (Holler et al. 2021), Haumea (Ragozzine & Brown 2009), Makemake (Parker et al. 2016), Gonggong (Kiss et al. 2017), Quaoar (Fraser et al. 2013), Orcus (Sickafoose et al. 2019), and Salacia (Stansberry et al. 2012), with Sedna being the exception.

It is clear that the current picture is that the Kuiper Belt should be densely populated with binary systems. The largest objects tend to be orbited by smaller moons, whereas roughly equal-sized binaries are expected at smaller sizes, with preference for tight orbits. However, the current collection of known TNBs clearly lacks these tight systems: Of the 144 known TNBs, only 5 (3.5 %) have separations below 800 km, whereas 52 (36.1 %) have separations less than 3000 km. The reason behind these numbers is an observational bias because most TNBs are discovered via direct imaging with the Hubble Space Telescope (HST) (Noll et al. 2020). The pixel scale of the Wide Field Camera 3 (WFC3), which is the optimal HST instrument for TNB detection, is 40 mas/pixel, equivalent to ~ 1200 km at 40 AU. With the most advanced point spread function fitting methods, binaries can be detected as close as half a WFC3 pixel (~ 600 km at 40 AU), although this is only possible for equal-sized TNBs with a combined brightness of $V \approx 21$. The resolution quickly degrades for fainter TNOs (see Figure 3 in Porter et al. (2024)).

HST observations are further constrained by several operational and environmental factors. Reliable target acquisition requires the availability of suitable guide stars within the limited guide-star patrol field, a condition that is not always met for TNO observations. In addition, when TNOs are projected against densely populated stellar fields (such as during passages near the Galactic plane) source confusion and background contamination might render the data unuseful. These conditions reduce sensitivity to close binaries and may therefore limit the suitability or prioritisation of such targets for HST observations.

The goal of this paper is to overcome the limitations of direct imaging in the search for TNBs. To do so, we have developed a methodology to quantitatively exploit the combination of thermal data and stellar occultation measurements. This methodology allows us to indirectly infer the presence of satellites around TNOs independently of the separation distance, as long as the system is unresolved. The basic idea is to include occultation derived sizes in the analysis of mid- and far-infrared measurements. It has been observed that the occultation diameters, which are direct measurements, tend to be slightly smaller than those obtained by fitting single-object models to thermal data. This difference can be attributed to the presence of an unresolved companion, whose flux also contributes to the infrared measurements (Ortiz 2020). Consequently, when a single-object thermal model is fitted to these measurements, an artificially larger diameter is obtained to account for the extra thermal emission from the satellite.

The "TNOs are Cool" project (Müller et al. 2009) was a *Herschel Space Observatory* open time key programme dedicated to observing the thermal emission of TNOs and Centaurs. This programme also incorporated measurements from *Spitzer*. A total of 180 objects were observed under this programme (Müller et al. 2020). Radiometric sizes and albedos have been published for most of these objects from fits of the Near Earth Asteroid Thermal Model (NEATM, Harris (1998)), or slight modifications to it. It is important to note that these results come from considering a single object. In this paper, we use the colour corrected

mid- and far-infrared measurements from "TNOs are Cool" publications.

Stellar occultations offer a way of determining sizes of Solar System bodies with kilometric accuracy (Ortiz et al. 2020b). For the first time, a significant sample of TNOs with a direct size measurement is available. Some of them were also targets of "TNOs are Cool". Hence, we are in conditions to combine these datasets and set the first preliminary constraints on the presence of satellites among these bodies, free of the separation bias.

This work is structured as follows: In Section 2 we describe in detail the modelling we implemented and the Bayesian approach that is followed for parameter determination. In Section 3 we describe the TNOs that will be analysed with this methodology. In Section 4 we expose the datasets used. The concrete application of the aforementioned methodology to our target selection is detailed in Section 5 and the results are presented and discussed in Section 6.

2. Methodology

In the original "TNOs are Cool" works, a single-object model is considered by default. In this paper, we use the NEATM (Harris 1998) to model both components of a TNB. Application of the NEATM to TNOs has been extensively discussed in many of the "TNOs are Cool" publications (e. g. Vilenius et al. 2012, Santos-Sanz et al. 2012). In Gómez-Limón et al. (2025), a binary object model consisting in two NEATM bodies was applied for the first time to model the thermal emission of a TNO in combination with occultation measurements. In this Section, we present an improved methodology based on the one presented in that paper which will be applied to the selection of TNOs specified in Section 3.

2.1. The model

The NEATM assumes a spherical object in the limit of zero thermal inertia and/or no rotation. In other words, the temperature at each surface point only depends on the solar illumination geometry. Therefore, the temperature distribution on the surface of the sphere is given by (Delbo et al. 2007)

$$T = \begin{cases} T_{SS}(\cos i)^{1/4}, & \text{if } i < \pi/2. \\ 0, & \text{if } i > \pi/2. \end{cases} \quad (1)$$

Here i is the angular distance of a surface point to the sub-solar point² and T_{SS} is the temperature at the sub-solar point. The value of the sub-solar temperature is determined by equating the total energy absorbed by a surface element to that emitted in the thermal infrared. A factor η , known as the beaming parameter, is included in the energy balance equation to account for deviations from the assumptions (like the thermal inertia not being negligible). The expression for the sub-solar temperature is then (Delbo et al. 2007)

$$T_{SS} = \left[\frac{(1 - A)S_{\odot}}{\epsilon\eta\sigma(r_h/1 \text{ AU})^2} \right]^{1/4}, \quad (2)$$

where A is the Bond albedo, $S_{\odot} = 1367 \text{ W m}^{-2}$ is the solar constant (Thuillier et al. 2004), σ is the Stefan-Boltzmann constant, ϵ is the emissivity, and r_h is the heliocentric distance of the modelled object. Throughout this work, a grey emissivity ($\epsilon = 0.9$) is assumed, as has been the case for the publications of "TNOs

² Point where solar radiation is normal to the surface.

are Cool" (Lellouch et al. (2013)). Since the solar spectrum peaks near the V-band, we assume $A \simeq A_V = qp_V$. Here, q is the phase integral and p_V is the geometric albedo (in the V-band). For consistency with the TNOs are Cool studies, we adopt the same approximation for the phase integral ($q = 0.336p_V + 0.479$; Brucker et al. 2009). We note that more recent determinations of phase integrals for TNOs exist (Verbiscer et al. 2022), but we retain this formulation to ensure direct comparability.

The disc integrated flux is then computed in the NEATM by assuming grey-body radiation at each surface element visible to the observer. The phase angle is taken into account, although its effect is almost negligible for TNOs since they are always observed at very small phase angle from Earth's perspective. The value of this integral depends on the diameter of the sphere D_{eq} . Therefore, for a single object, the observed flux at a certain thermal wavelength under the NEATM is a function only of the beaming parameter η , the geometric albedo p_V and the object diameter D_{eq} .

From the definition of absolute magnitude H_V for a Solar System body, the geometric albedo is given by

$$p_V = \frac{\pi a^2}{S_{\text{proj}}} 10^{\frac{2}{5}(V_{\odot} - H_V)}, \quad (3)$$

where $a = 1$ AU, $V_{\odot} = -26.76 \pm 0.02$ mag is the apparent V magnitude of the Sun (Bessell et al. 1998) and S_{proj} is the projected area towards the observer, which for a spherical model is $S_{\text{proj}} = \pi D_{\text{eq}}^2/4$. Using Eq. 3, one can exchange the dependency of NEATM on p_V for dependency on H_V . Consequently, for a single object, we have $F_{\text{model}}(\lambda) = F_{\text{NEATM}}(H_V, D_{\text{eq}}, \eta; \lambda)$.

In the present work, we assume that both components of the binary system are unresolved. This implies that measurements of the absolute magnitude represent the brightness of the combined system. We adopt a model where both components have equal surface properties, i.e., equal beaming parameter and geometric albedo. Given the diameters of the primary D_{eq} and secondary d_{eq} and the combined absolute magnitude H_V , one can compute the projected area of the combined system $S_{\text{proj}} = \pi(d_{\text{eq}}^2 + D_{\text{eq}}^2)/4$ and use Eq. 3 to retrieve the common albedo for both objects. Once p_V is known, we can invert Eq. 3 to obtain the individual absolute magnitudes $H_{V,\text{main}}$ and $H_{V,\text{sat}}$. Hence, we can write for the combined system:

$$F_{\text{model}}(\lambda) = F_{\text{NEATM}}(H_{V,\text{sat}}(H_V, D_{\text{eq}}, d_{\text{eq}}), d_{\text{eq}}, \eta; \lambda) + F_{\text{NEATM}}(H_{V,\text{main}}(H_V, D_{\text{eq}}, d_{\text{eq}}), D_{\text{eq}}, \eta; \lambda). \quad (4)$$

In the present work, we use the available direct measurements of H_V and D_{eq} in the literature. The absolute magnitude measurements come from regular ground-based photometric observations. For the diameter of the primary, we use occultation data. In general, the detected projected limbs are not circular, and ellipses are fitted to the observed occultation chords in the literature. To assign a diameter value to the occultation measurement, we use the area-equivalent diameter, i.e., the diameter of a circle of equal area to the fitted ellipse.

All the occultation data used in this work correspond to detections of a single object. We assume that the detected object is the largest component of the pair in case the object is actually a binary system. This is the most likely situation, since smaller satellites might lie undetected in between chords or outside the scanned area of the sky plane. However, nowhere on the previous equations is imposed that $d_{\text{eq}} < D_{\text{eq}}$, so this modelling can also be applied in the case where the detected object is the

secondary/satellite (in which case d_{eq} and D_{eq} would exchange roles).

Since H_V and D_{eq} have known values, from Eq. 4 it is clear that we only have η and d_{eq} as free parameters to model the observed flux at certain thermal wavelength λ .

2.2. Bayesian statistical approach

We follow a Bayesian approach for parameter estimation. We choose this methodology because it is the most appropriate way to propagate the uncertainties in D_{eq} and H_V in our analysis. Bayesian parameter estimation also allows for a full characterisation of uncertainties and parameter correlation, and allows computing credible intervals or upper limits on the parameter values in a natural way.

The central goal of Bayesian inference is to characterise the posterior probability density function (posterior pdf or simply posterior). This distribution describes the conditional probability of the model parameters $\theta = (d_{\text{eq}}, \eta)$ given the measured thermal fluxes $\mathcal{D} = \{F_{\text{meas}}(\lambda_i)\}_i$ and considering our prior knowledge of the parameters. According to the Bayes Theorem, the posterior $P(\theta|\mathcal{D})$ can be expressed as

$$P(\theta|\mathcal{D}) = \frac{\mathcal{L}(\mathcal{D}|\theta)P(\theta)}{P(\mathcal{D})}, \quad (5)$$

where $\mathcal{L}(\mathcal{D}|\theta)$ is the likelihood function, $P(\theta)$ is the prior pdf and $P(\mathcal{D})$ is known as the evidence (Gelman et al. 2013; Robert 2007).

$P(\theta)$ represents our belief on the parameter values prior to the measurements whose analysis will result in an update on such beliefs. We assume that, a priori, η and d_{eq} are independent, and hence the prior pdf can be written as $P(\theta) = f_1(\eta)f_2(d_{\text{eq}}; H_V, D_{\text{eq}})$.

The likelihood function $\mathcal{L}(\mathcal{D}|\theta)$ measures how likely it is to observe the data \mathcal{D} for different parameter values θ . In our case, the data are the flux measurements at thermal wavelengths from "TNOs are Cool". We consider that the flux errors σ_i are independent and normally distributed, in which case the likelihood may be written as (Gregory 2005):

$$\mathcal{L}(\mathcal{D}|\theta) = (2\pi)^{-N/2} \left[\prod_{i=1}^N \frac{1}{\sigma_i} \right] \exp \left[- \sum_{i=1}^N \frac{[F_{\text{meas}}(\lambda_i) - F_{\text{model}}(\lambda_i)]^2}{2\sigma_i^2} \right] \quad (6)$$

Estimates on the value of the beaming parameter are given for all our targets in previous "TNOs are Cool" publications. However, these estimates are based on the fitting of single-object models. Consequently, we cannot use these values individually as prior information for each of our targets, since we are considering a binary object model. Instead, we choose to use for every target the distribution of η values across the TNO population. We take the 68 beaming parameter values fitted in Lellouch et al. (2013) (TNOs only) and estimate $f_1(\eta)$ using Gaussian Kernel Density Estimation with the `gaussian_kde` class of `scipy.stats` Python package.

For the prior in the diameter of the secondary, we consider a uniform distribution for all targets. Some of our targets have known satellites (see Section 3), and size estimates are available in the literature. However, we ignore this information in our analysis so that these objects serve as validation for our methodology. The limits of the uniform distribution d_{low} and d_{high} depend on the nominal values of the occultation derived diameter D_{eq} and

the absolute magnitude of the system H_V . In general, if the common geometric albedo p_V is known, one can infer the value of d_{eq} by computing $H_{V,\text{main}}$ from Eq. 3, then obtaining $H_{V,\text{sat}}$ from $H_{V,\text{main}}$ and H_V , and finally applying Eq. 3 again. d_{low} is the result of this computation if one assumes $p_V = 0.01$ and d_{high} is the result if $p_V = 1.15$. In practice, this does not exclude a priori any reasonable d_{eq} values. However, imposing these limits is necessary to ensure no extreme p_V values are internally encountered in the sampling process. Summing up, we choose $f_2(d_{\text{eq}}; H_V, D_{\text{eq}})$ to be the pdf of a uniform distribution between $d_{\text{low}}(H_V, D_{\text{eq}})$ and $d_{\text{high}}(H_V, D_{\text{eq}})$, reflecting that we have no a priori information on the size of any putative companion, except that the albedo cannot be extreme.

To approximate the posterior distribution, we employ a Markov Chain Monte Carlo (MCMC) method to generate samples from it. For this purpose, we use the Python package `emcee` 3.1.6 (Foreman-Mackey et al. 2013), which implements the affine invariant sampling algorithm described in Goodman & Weare (2010).

In each of our MCMC samplings, we used `emcee` with $n_w = 128$ random walkers (i.e. parallel chains in the ensemble sampler), running the sampler for $n_{\text{burn}} = 500$ initial steps. The samples from the initial steps are subsequently discarded (burn-in phase), in order to reduce the influence of the initial conditions before the chains reach their stationary distribution. We adopt the criterion $n_{\text{burn}} \geq 10\tau$ in both d_{eq} and η , where τ is auto-correlation time estimated by `emcee`. The criterion ensures that the chain is evolved long enough to effectively lose dependence of its initial state. Starting from the last position of the burn-in phase, the sampler is run for n_{iter} additional iterations. The sample size from this final phase is therefore $n_w \times n_{\text{iter}}$, which is representative of the posterior distribution $P(\theta|\mathcal{D})$. For a comprehensive explanation of these criteria and parameters, we refer the reader to the original `emcee` papers and references therein.

To propagate the uncertainties in the values of H_V and D_{eq} , which have been independently directly measured, we choose a scheme in which we perform a total of 500 MCMC runs for each analysed object. These runs are the result of dividing the $D_{\text{eq}} \times H_V$ parameter subspace in a grid, and performing each run with a fixed value combination of (D_{eq}, H_V) in the generation of our modelled fluxes with Eq. 4. To generate the grid, we draw $n = 500000$ (H_V, D_{eq}) pairs from the uncertainty distributions of H_V and D_{eq} , considering the variables are independent. In most cases, the literature values report a symmetric error bar, in which case we consider a normal distribution with σ equal to the reported error. From this sample, we then perform a bidimensional histogram of 500 equal-sized bins; 50 bins for the case of D_{eq} and 10 bins for the case of H_V . We have a lower resolution in the absolute magnitude dimension because d_{eq} (the parameter we are most interested in) shows low dependency on H_V , see Section 6.11.

In each 2D bin, we run the burn-in phase, and the number of additional steps n_{iter} is proportional to the number of counts in the bin m_{bin} : $n_{\text{iter}} = \lfloor m_{\text{bin}}/n_w \rfloor$. Then we combine all 500 samples into a single one, incorporating the (H_V, D_{eq}) values for each of them. Therefore, the final sample will consist of n four-dimensional vectors $(H_V, D_{\text{eq}}, d_{\text{eq}}, \eta)$, where only the knowledge of d_{eq} and η is being updated in this Bayesian scheme.

3. Sample selection

Our basic target selection criterion is that the TNO should have published thermal emission and occultation measurements. We

restricted to occultations with at least three positive chords, so that a reliable projected area can be retrieved.

We explicitly excluded the remarkable cases of Quaoar and Haumea, since they are bodies known to possess rings (Ortiz et al. 2017; Morgado et al. 2023), a feature that is not considered in our model and which would lead to systematic errors in the analysis. On top of this, these objects have already been thermophysically modelled in detail, see Kiss et al. (2024b) and Santos-Sanz et al. (2017) respectively. Similarly, Makemake is also excluded from our analysis. It is a system with complex thermal emission (Kiss et al. 2024a) and for which intricate two-terrain thermal models have been applied in the past (Lim et al. 2010). Eris is also excluded because, although it technically has a three positive chord occultation, two of the chords correspond to telescopes located in the same observatory. Therefore, the area-equivalent diameter is poorly constrained, as it might vary from ~ 2300 km from a circular fit to ~ 3000 km from an elliptical fit (Sicardy et al. 2011).

(143707) 2003 UY117 is a "TNOs are Cool" target with a published three-chord occultation (Kretlow et al. 2024). However, the thermal emission coverage is very poor, as it was only observed at $70 \mu\text{m}$ and $160 \mu\text{m}$, and for the latter the emission was so low that only an upper limit in flux is reported (Farkas-Takács et al. 2020). Therefore, we also exclude this object from our study.

The rest of TNOs fulfilling the aforementioned criterion are included in our target selection and are listed on Table 1. We have a sample of ten TNOs of diverse dynamical classes, four of which are already known binary systems:

- (208996) Achlys (provisional designation 2003 AZ84) has a satellite 5.0 ± 0.3 magnitudes fainter than the primary, discovered from HST (Brown & Suer 2007). Assuming equal albedos for primary and secondary, measurements of the primary by stellar occultations deliver an approximate size for the secondary of ~ 80 km in diameter (Dias-Oliveira et al. 2017). The semi-major axis of the orbit is roughly 7200 km, corresponding to < 300 mas of projected separation at Achlys distance.
- (229762) G!kún||hòmdímà (provisional designation 2007 UK126) is a system extensively studied with HST data (Grundy et al. 2019a). Its satellite G!d'él!hú is 3.242 ± 0.039 magnitudes fainter. The semi-major axis of the orbit is well constrained to be $a = 6035 \pm 48$ km, equivalent to < 250 mas at its distance.
- The satellite of (38628) Huya (provisional designation 2000 EB173) was discovered using HST in 2012 (Noll et al. 2012). Stellar occultations by the satellite provide a very reliable lower limit for its size, set to $d_{\text{sat}} > 165$ km in Rommel et al. (2025). From the same work, the semi-major axis of the orbit is determined to be $a = 1898^{+22}_{-22}$ km (< 100 mas of separation), being the tightest known binary system in our sample.
- (174567) Varda (provisional designation 2003 MW12) has a large satellite named Ilmarë, which has also been extensively studied from HST and other large ground-based telescopes (Grundy et al. 2015). These observations allowed the fitting of the orbit, resulting in a semi-major axis of $a = 4812 \pm 35$ km, or < 200 mas at Varda's distance. The observed magnitude difference in the system is $\Delta m = 1.734 \pm 0.042$ (Grundy et al. 2015).

The previous four systems serve as validation of the methodology. To first order, the presence of a satellite should be recovered in these cases, corroborating that similar satellites should

also be recovered in the case of smaller separation distances. To second order, we can verify if the satellite diameter derived from our methodology is compatible with the estimations done with independent measurements.

It is important to note that, in all four cases, the maximum apparent separation from Earth is well below 0.5 arcsec. Since the average seeing from the ground is over 0.5 arcsec in the overwhelming majority of situations, the photometric observations of these targets from the ground will measure the blended flux of both the main body and the satellite (unless adaptive optics are used). In other words, the system is unresolved in ground-based observations without adaptive optics, as those used to obtain the absolute magnitude of the objects. Therefore, the values in the literature reflected in Table 1 take into account the combined flux of both bodies. The spatial resolution of *Herschel*/PACS and *Spitzer*/MIPS is ~ 5 arcsec or worse (Rieke et al. 2004; Poglitsch et al. 2010). Consequently, the thermal measurements also represent the combined infrared flux of the system.

Currently, we do not have direct evidence that the remaining TNOs in our target list (84522, 119951, Máni, 84922, Ixion and 470316) possess any satellite. However, it must be noted that these objects have been studied non-homogeneously with HST. We performed a search in the Mikulski Archive for Space Telescopes (MAST³) taking into account provisional designation, permanent designation and numbering of the objects. According to this search:

- The objects 84522, 119951, Máni, 84922, and Ixion have been observed under the HST proposal ID 10545. One image was taken for 84522, four for Ixion, and two for the other objects. The aim of the proposal was to discover and characterise satellites around TNOs using the Advanced Camera for Surveys (ACS) instrument. No detections were ever reported for these targets.
- Ixion was also observed under the HST proposal ID 9110, with a similar goal of discovering Charon-analogue satellites. Ixion observations consisted of two images using the Space Telescope Imaging Spectrograph (STIS) instrument. No satellite has been reported.
- We found no HST observations for 470316.

4. Observational data

A summary of the D_{eq} and H_V values used and the corresponding references can be found in Table 1. In the following, we give some details on the particularities of each target. Specifically, we report the mid- and far-infrared wavelength coverage by "TNOs are Cool" measurements and the corresponding sources. We take the flux values and uncertainties as they are. We also take from these sources the relevant geometrical parameters from the observations: target-observer distance, heliocentric distance, and phase angles. The coverage can include two bands from *Spitzer*/MIPS centred at 24 μm and 71 μm , and three bands from *Herschel*/PACS at 70 μm , 100 μm and 160 μm . Exceptionally, some "TNOs are Cool" targets were also observed with *Herschel*/SPIRE (bands at 250 μm , 350 μm and 500 μm).

4.1. (208996) Achlys

The case of Achlys is of special interest. (Dias-Oliveira et al. 2017) report two multi-chord occultations by this TNO, with 3 positives each. The fitted projected ellipses are considerably

different, both in eccentricity and size. In Dias-Oliveira et al. (2017), the authors argue that this represents a triaxial body observed at two different rotational phases. A Jacobi ellipsoid is fitted to these projections and the observed rotational light curve amplitude. A mean area-equivalent diameter of 772 ± 12 km is reported (rotational average) for the derived three-dimensional shape. We implement this D_{eq} value in our analysis.

Achlys was intensively observed with *Herschel*/PACS within the "TNOs are Cool" programme. The objective was to measure its rotational light curve at thermal wavelengths, although this was not achieved (Santos-Sanz et al. 2017). In this work we use the averaged *Herschel*/PACS values reported in Table 2 from Mommert et al. (2012). These do not include measurements at 70 μm . We also take the *Spitzer*/MIPS measurements from the same publication.

4.2. (229762) G!kún||'hòmdímà

G!kún||'hòmdímà produced a stellar occultation in 2014 (8 positive chords) that has been analysed in Schindler et al. (2017) and in Benedetti-Rossi et al. (2016). In Schindler et al. (2017) only 3 chords are used in the analysis of the projected shape (well spaced and with reliable GPS timings), although the resulting fitted ellipse is almost identical to that reported in Benedetti-Rossi et al. (2016), which uses more chords. We decide to use as area-equivalent diameter the one from Schindler et al. (2017) because the authors used only the data with highest timing accuracy. In this work, also volume-equivalent diameter estimates are provided. However, in this case we decided not to use these values since they are informed by the same thermal data we use here, but assuming a single-object model.

Flux measurements in the three *Herschel*/PACS bands are available for this object (Santos-Sanz et al. 2012). Schindler et al. (2017) revisit the originally published values, and re-reduce the data following the technique described in Kiss et al. (2014). Because of the higher SNR and improved calibration using stars of similar brightness to the target, we use these revised data as our thermal dataset.

The absolute magnitude of the system is also revised in Schindler et al. (2017). The reported value is the same as in Perna et al. (2010), but with larger uncertainty that takes into account effects from potential rotational variability. This H_V value incorporates the flux contribution from the satellite G!ò'éhú.

4.3. (38628) Huya

Huya has two published multi-chord occultations, one from 2019 (Santos-Sanz et al. 2022) and one from 2023 (Rommel et al. 2025). In both cases, the observed projected area is very similar, with area-equivalent diameters of 411.0 ± 7.3 km and 420.6 ± 22.0 km respectively. Because of the almost unchanging observed projections, we stick with the value reported in Santos-Sanz et al. (2022) for our analysis, because the 2019 occultation has higher SNR in the occultation light curves, leading to a smaller uncertainty.

Fornasier et al. (2013) report thermal measurements for the two *Spitzer*/MIPS bands, the three *Herschel*/PACS bands, and also measurements at 250 μm , 350 μm and 500 μm from *Herschel*/SPIRE. ALMA observations of Huya at 1.29 mm (Lelouch et al. 2017) are also included in our analysis. This object exhibits the broadest thermal wavelength coverage among the TNOs in our sample.

³ <https://mast.stsci.edu/search/ui/#/>

4.4. (174567) Varda

Souami et al. (2020) report the only multi-chord occultation to date of Varda, with five positive chords. Fluxes in the three *Herschel*/PACS bands for Varda are available in Vilenius et al. (2014).

Two non-compatible absolute magnitudes of the Varda-Ilmarë system are reported in the literature. Vilenius et al. (2014) derive a value of $H_V = 3.61 \pm 0.05$ using data from Perna et al. (2013). Alvarez-Candal et al. (2016) estimate an absolute magnitude of $H_V = 3.998 \pm 0.048$ using literature data and including data from Observatorio de Sierra Nevada 1.5 m and Calar Alto 3.5 m telescopes. The main difference between the two works is that Vilenius et al. (2014) use a fixed phase coefficient equal to the mean of the TNO population (Belskaya et al. 2008), whereas Alvarez-Candal et al. (2016) fit the phase coefficient to their dataset. For this reason, we believe the latter is more reliable.

4.5. (84522) 2002 TC302

This object was successfully observed via a stellar occultation in 2018, with 12 positive detections (a record coverage at the time for a TNO besides Pluto). Its projected area at the moment of the occultation was determined with notable precision (Ortiz et al. 2020a).

Within the "TNOs are Cool" programme, it was observed with *Herschel*/PACS and *Spitzer*/MIPS. With MIPS, the flux at 71 μm could not be recovered because the object was merged with a background source, so only the flux at 24 μm is available (Fornasier et al. 2013).

The absolute magnitude value we use for this object is $H_V = 4.23$, reported in Tegler et al. (2016). However, they report no uncertainty, so we assume a conservative $\sigma_{H_V} = 0.1$ as they report colours for this object with $\sigma = 0.02$ mag.

4.6. (119951) 2002 KX14

The object 119951 is currently crossing the galactic plane and consequently has undergone numerous occultation events, several of which have multiple positive detections. In Rizos et al. (2025) a collection of 4 multi-chord events is published. Their analysis concludes that all the occultations are coherent, within uncertainties, to the same projected ellipse (the three dimensional shape is likely an oblate spheroid). In our analysis, we use the area-equivalent diameter from their elliptical fit to all the occultations events.

Thermal emission wavelength coverage of 119951 is extensive, with measurements in the three *Herschel*/PACS bands and the two *Spitzer*/MIPS bands (Vilenius et al. 2012).

4.7. (307261) Máni

Máni is currently the TNO with the most positive chords ever detected in an occultation: 61. The coverage was so comprehensive that even topographic features could be identified (Rommel et al. 2023). For the present work, we take the area-equivalent diameter from the global elliptical fit to a selection of chords (those with the most accurate timings) in Rommel et al. (2023), see their Table 4.

As was the case for 119951, the thermal emission wavelength coverage from *Herschel*/PACS and *Spitzer*/MIPS is complete (Vilenius et al. 2012).

4.8. (84922) 2003 VS2

The case of 84922 is similar to Achlys. It also has two published multi-chord stellar occultations, one in 2014 (Benedetti-Rossi et al. 2019) and one in 2019 (Vara-Lubiano et al. 2022). Its shape likely departs from a spheroid, since it has a large rotational light curve amplitude (Sheppard 2007; Ortiz et al. 2006). Because the rotational phase at the time of the 2019 occultation was exceptionally well constrained, in Vara-Lubiano et al. (2022) a mean area equivalent diameter is reported, which represents the rotational average. We use this value of $D_{\text{eq}} = 545 \pm 13$ km in our analysis.

As for Achlys, extensive observations of 84922 were carried out to look for rotational variation in the thermal emission (Santos-Sanz et al. 2017). As before, we consider the rotationally averaged flux values from *Herschel*/PACS reported in Table 2 from Mommert et al. (2012). In this case, the 100 μm band is not available. We also take the *Spitzer*/MIPS measurements from the same publication.

4.9. (28978) Ixion

The case of Ixion is similar to that of 119951, as it is also immersed in a region of the sky densely populated by stars. Therefore, several multi-chord occultations have been measured in recent years. A compilation of them has been published in Kilić et al. (2026). In this work, the authors follow a methodology similar to 119951 (Rizos et al. 2025): Since the projected profile seems to be unchanged across occultations, a single ellipse is fitted to all the combined occultations, leading to the area-equivalent diameter value presented in Table 1, that we incorporate to our analysis. Fluxes in the three *Herschel*/PACS bands for Ixion were published in Lellouch et al. (2013).

4.10. (470316) 2007 OC10

An occultation of a double star by 470316 in 2022 delivered 4 positive chords (Gómez-Limón et al. 2025). This object is the smallest in our sample, and also has the largest uncertainties in projected size due the moderate SNR in the occultation light curves. Because this object is the only object in our sample with an occultation analysed under a Bayesian framework, it is also the only one with asymmetrical error bars in the reported area-equivalent diameter.

Complete *Herschel*/PACS coverage of this object is available in Santos-Sanz et al. (2012). This object has already been analysed using a methodology almost identical to that proposed in Section 2, the only difference being that uncertainties in absolute magnitude were not considered (Gómez-Limón et al. 2025). Therefore, it serves as a useful test to check how our inference on putative satellite presence changes when introducing uncertainties in H_V .

5. Analysis

The parameter we are most interested in is the area-equivalent diameter of the satellite, d_{eq} . By analysing the marginalised posterior of d_{eq} we can distinguish between two cases:

1. The marginalised posterior peaks at $d_{\text{eq}} = 0$. In this case, according to our analysis, a single-object model is coherent with both thermal data and occultation observations. We can use this marginalised posterior to set quantitative upper limits on the presence of any companion. For example, the 68 %

Table 1: Summary of dynamical, physical, and rotational properties for the analyzed targets.

Object	Orbital Class	Known Binary	D_{eq} (km)	H_V (mag)	Rot. LC amplitude (mag)
(208996) Achlys	Plutino	Yes	772 ± 12 (D17)	3.779 ± 0.114 (A16)	0.07 ± 0.01 (T10)
(229762) G!kún hòmdímà	Detached	Yes	621 ± 7 (S17)	3.69 ± 0.10 (S17)	0.03 ± 0.01 (T14)
(38628) Huya	Plutino	Yes	411.0 ± 7.1 (S22)	5.04 ± 0.03 (F13)	0.02 ± 0.01 (T14)
(174567) Varda	Resonant 15:8	Yes	740 ± 14 (S20)	3.998 ± 0.048 (A16)	0.02 ± 0.01 (T14)
(84522) 2002 TC302	Resonant 5:2	No	500 ± 10 (O20)	4.23 ± 0.10 (T16)	0.06 ± 0.01 (O20)
(119951) 2002 KX14	Classical *	No	382.2 ± 8.7 (R25)	4.978 ± 0.017 (A16)	< 0.05 (R25)
(307261) Máni	Hot Classical	No	796 ± 24 (R23)	3.63 ± 0.05 (R23)	0.05 ± 0.01 (T13)
(84922) 2003 VS2	Plutino	No	545 ± 13 (V22)	4.14 ± 0.07 (A16)	0.264 ± 0.017 (V22)
(28978) Ixion	Plutino	No	697 ± 10 (K26)	3.845 ± 0.006 (K26)	< 0.15 (O03)
(470316) 2007 OC10	Detached	No	330^{+56}_{-55} (G25)	5.40 ± 0.02 (G25)	< 0.1 (G25)

Notes. Orbital classification follows Volk & Van Laerhoven (2024). * Classification of 119951 as hot or cold classical is debated (Fernández-Valenzuela et al. 2021; Rizos et al. 2025). The values of primary area-equivalent diameter and system absolute magnitude used in our analyses are the ones listed in the D_{eq} and H_V columns respectively. For thermal measurements sources, please refer to Section 4.

References. (A16) Alvarez-Candal et al. (2016); (D17) Dias-Oliveira et al. (2017); (F13) Fornasier et al. (2013); (G25) Gómez-Limón et al. (2025); (K26) Kilic et al. (2026); (O03) Ortiz et al. (2003); (O20) Ortiz et al. (2020a); (R23) Rommel et al. (2023); (R25) Rizos et al. (2025); (S17) Schindler et al. (2017); (S20) Souami et al. (2020); (S22) Santos-Sanz et al. (2022); (T10) Thirouin et al. (2010); (T13) Thirouin (2013); (T14) Thirouin et al. (2014); (T16) Tegler et al. (2016); (V22) Vara-Lubiano et al. (2022).

credibility upper limit is given by the 68 % quantile. Our inference on the beaming parameter for these cases can be directly compared to the results from "TNOs are Cool" works, where a single-object model is assumed by default (in Lelouch et al. (2013), for example). Our result will represent an updated value since "TNOs are Cool" analyses feature D_{eq} as a free parameter to be fitted, whereas we adopt the diameter independently derived from occultations.

- The marginalised posterior shows a peak at $d_{\text{eq}} > 0$. In this case, the conclusion is that a binary object explains better the occultation and thermal data. We give an estimate of the size of the putative satellite by reporting the mean of the marginalised posterior in d_{eq} . The corresponding error bars are computed by taking the 68 % maximum density credible interval in this marginalised posterior. That is, the shortest interval containing 68 % of the sample elements, corresponding to the 1σ region.

We flag these two cases for our targets in the the second column in Table 2. For all targets, the nominal value of η is reported as the median of the marginalised sample, and the error bar is computed from the 68 % maximum density credible interval.

6. Results and Discussion

Our results are summarised in Table 2. In Figure 1 we graphically represent the obtained satellite sizes. The pairwise plots for the obtained posterior samples are shown in Figure 2 for the validation targets and in Figure 3 for the remaining targets. Plots showing the measured thermal fluxes against the modelled thermal spectral energy distribution are presented in Appendix B.

6.1. (208996) Achlys

We infer the presence of a companion for Achlys. This is consistent with the fact that Achlys has a known satellite, see Section 3. However, the estimated satellite diameter of 77^{+10}_{-11} km

from the observed magnitude difference (Dias-Oliveira et al. 2017) is smaller than the value obtained with our methodology $d_{\text{eq}} = 236^{+64}_{-52}$ km. It is important to note that we do not impose a difference in brightness between the primary and the secondary in our methodology. HST measured it to be of $\Delta m = 5.0 \pm 0.3$ magnitudes, whereas our results imply $\Delta m = 2.6^{+0.7}_{-0.5}$ mag. We hypothesise three scenarios to solve this discrepancy. The first one is that there is a considerable difference in albedos and/or beaming parameters between Achlys' main body and the satellite, whereas in our modelling we consider equal surface properties for both objects. The second one is that Achlys' rotationally averaged area-equivalent diameter has been underestimated by 5%. This would propagate to a nominally inferred satellite size of 85 km, given the negative correlation between D_{eq} and d_{eq} observed in our posterior sample. Finally, it might be the case that there is a second previously undetected satellite in the system. In our modelling, to account for the extra flux from this putative second satellite we need a larger value of d_{eq} .

6.2. (229762) G!kún||hòmdímà

For G!kún||hòmdímà our analysis yields a marginalized posterior in d_{eq} peaking at 0. We rule out the presence of any satellite above 159.1 km in diameter with 68% credibility, and above 258.8 km in diameter with 90% credibility. G!d'è!hú, the known satellite of G!kún||hòmdímà, is estimated to be 139.5 ± 2.9 km in diameter from the magnitude difference reported in Grundy et al. (2019a) and the observed size of G!kún||hòmdímà from occultations (assuming equal albedos), which is consistent with our derived 68% credibility upper limit.

This is the only target with a known satellite for which we do not recover its presence. The scarce thermal wavelength coverage, with only *Herschel*/PACS data, leads to a wide d_{eq} marginalised posterior pdf, preventing us from setting tighter constraints.

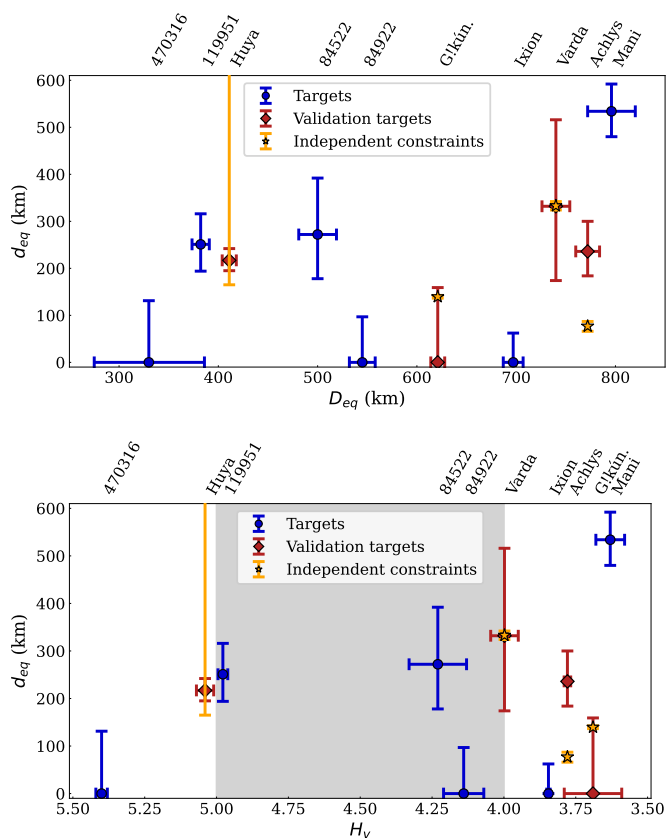


Fig. 1: Inferred satellite sizes for the target sample. The upper panel displays satellite size as a function of the primary’s occultation-derived area-equivalent diameter. The lower panel shows satellite size as a function of the system absolute magnitude obtained from independent photometric observations. The interval $H_V \in [4, 5]$, region where a dearth of binaries has been reported in Lyra (2025), is depicted in grey. For Huya, the independent upper limit on d_{eq} is represented with the orange error bar.

6.3. (38628) Huya

For Huya we infer the presence of a satellite 217^{+25}_{-22} km in diameter. The marginalised posterior in d_{eq} shows a negligible posterior probability of the satellite being smaller than 100 km in diameter (see Figure 2). This is the TNO in our sample with smallest uncertainties in d_{eq} for those falling in case 2 of the distinction made in Section 5. The size of the satellite obtained in this work is in agreement with the lower limit of 165 km reported in Rommel et al. (2025), from direct measurements with stellar occultations.

6.4. (174567) Varda

With Varda, we predict the presence of a satellite of size $d_{\text{eq}} = 332^{+181}_{-158}$ km. The 1σ credible interval in d_{eq} spans more than 300 km, and the corresponding marginalised posterior does not drop to 0 approaching $d_{\text{eq}} = 0$, see Figure 2. The results are less conclusive in this case than for other objects, since the thermal data wavelength coverage is narrower, lacking *Spitzer*/*MIPS* and *Herschel*/*SPIRE* measurements. In spite of this, the result is compatible with the estimated size of the known satellite Ilmarë,

of $332.9^{+9.1}_{-8.8}$ km in diameter from the difference in magnitudes reported in Grundy et al. (2015).

6.5. (84522) 2002 TC302

The occultation by 84522 revealed an area-equivalent diameter ~ 84 km smaller than that inferred by the fitting of a single-object NEATM model to the thermal data (Ortiz et al. 2020a; Fornasier et al. 2013). It has been suggested that this difference could be attributed to an undetected satellite. By simply equating $D_{\text{eq, occ}}^2 + d_{\text{eq}}^2 = D_{\text{eq, thermal}}^2$, a rough estimate of the size of 100-300 km was given in Ortiz et al. (2020a) for this putative satellite. From our more rigorous analysis, we obtain a 1σ credible interval for d_{eq} of [179, 386] km, reasonably compatible with this previous estimate.

In Ortiz et al. (2020a), the effects of a putative satellite in this size range on the short term photometry and astrometric residuals are explored. They conclude that a ~ 200 km secondary could account for the dispersion observed in the astrometric residuals and the observed rotational photometric variability. In the same work, the authors report that the observational coverage in the cross-track direction away from the main body was poor. Therefore, a satellite in the proposed size range could have easily been missed.

It is worth noting that the posterior pdf is non-zero for $d_{\text{eq}} = 0$, see Figure 3. This indicates that our analysis is not completely incompatible with 84522 being a single object, although the presence of a sizeable satellite is more likely.

6.6. (119951) 2002 KX14

Similarly to the case of 84522, the area-equivalent diameter from occultation data is found to be ~ 65 km smaller than that from single-object model fitted to thermal measurements (Rizos et al. 2025). In our analysis, the presence of a sizeable satellite is inferred, with a credible interval of 1σ for its diameter of [194, 316] km. In this case, the marginal posterior in d_{eq} is almost zero for small d_{eq} values (see Figure 3), which means that evidence for the presence of a putative satellite is strong according to our methodology. Our modelling of this TNO shows a remarkably good fit to the thermal data, see Figure B.2.

Four different occultations have been observed for this object, and none show secondary detections compatible with such a satellite. Nevertheless, the positive chords always scan 119951’s sky plane in almost the same direction (see Fig. B.6 in Rizos et al. (2025)), and there are in total only two negative observations constraining the surroundings of the body.

6.7. (307261) Máni

This object shows the largest deviation between the diameter estimated from thermal data (single-object modelling) and the diameter directly measured from occultations, being the latter ~ 138 km smaller than the former (Rommel et al. 2023). According to our analysis, it is also the object that should have the largest companion; the inferred 1σ credible interval is [480, 592] km, roughly two thirds of the diameter of the main body. Our posterior estimations strongly suggest that a large satellite should be present, as $P(\theta|\mathcal{D})$ is almost null for $d_{\text{eq}} < 300$ km, see Figure 3.

Máni has unprecedented occultation data coverage. Nine occultations are published in Rommel et al. (2023), where three are single-chord, four are double-chord and two are multi-chord,

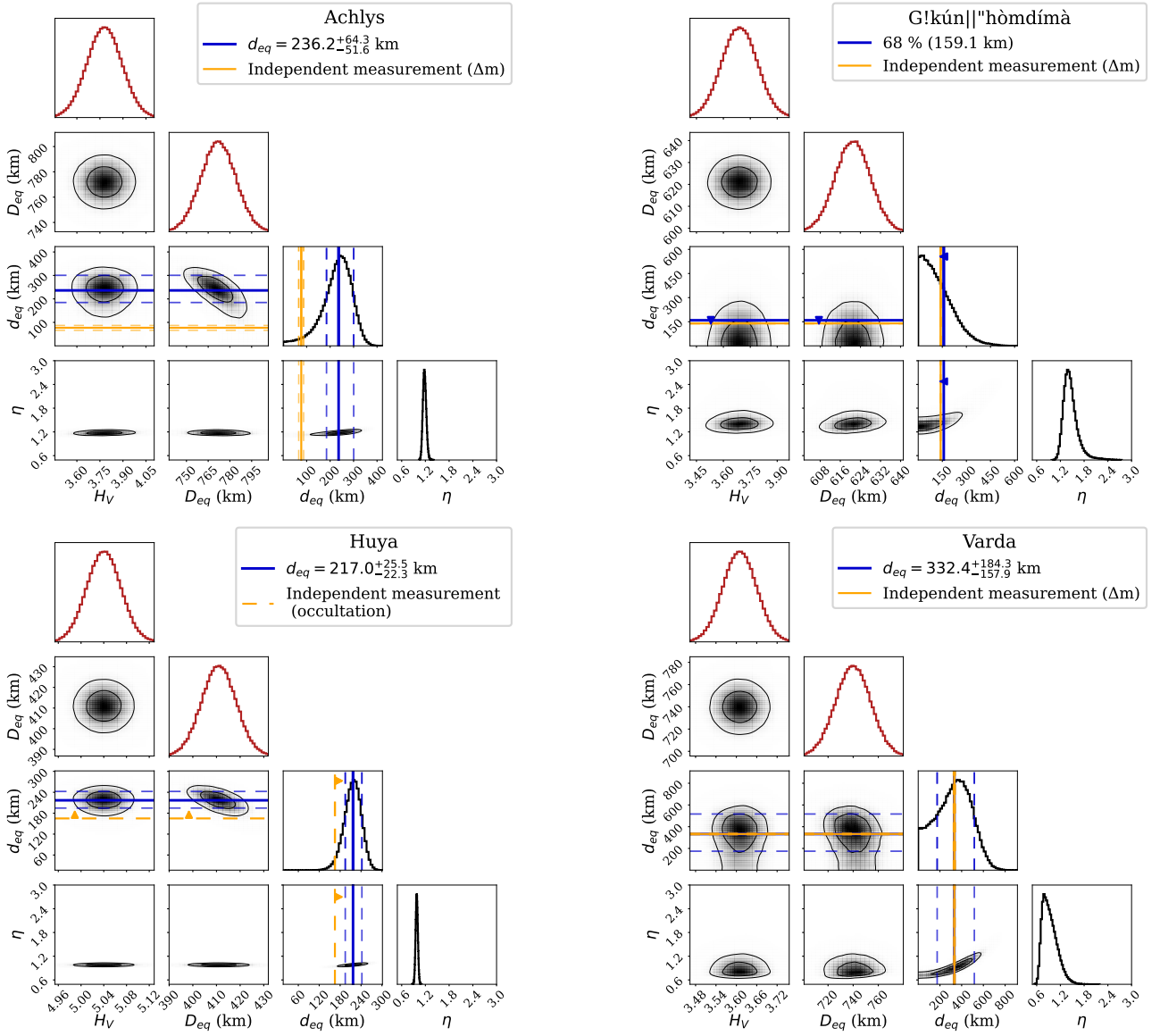


Fig. 2: Pairwise plots for the validation targets. The marginalised posterior pdfs of H_V and D_{eq} are shown in red to highlight the fact that these are not free parameters. These pdfs represent the independent measurements of H_V and D_{eq} from literature, reported in Table 1, that were included in the analysis. The constraints on the size of the satellite from independent measurements are overplotted in yellow, see Table 2. Except for Huya, these independent constraints come from the observed magnitude difference, which we translate into a secondary area-equivalent diameters under the assumption of equal albedos. The propagated uncertainties for these diameters (dashed yellow lines) are small. In some plots they are almost indistinguishable from the nominal value (solid yellow line).

with three and 61 positive detections respectively. However, no secondary features compatible with a satellite are detected. The surroundings of the main body are explored with great resolution in the event with 61 positives (8 August 2022), as many negative light curves are available near the main detection. These negatives scan an area 900 km to the South and 1100 km to the North from the centre of the detected (main) body, see (Rommel et al. 2023, Figure 3). Similarly, the along-track coverage also covers more than 1000 km East and West of the main body. The chords show spacings of, at most, ~ 200 km between them.

6.8. (84922) 2003 VS2

For 84922, we obtain a marginalised posterior in d_{eq} peaking at 0, see Figure 3. Therefore, we derive an upper limit on the presence of a putative companion. We rule out the presence of any satellite above 97 km in diameter with 68% credibility, and above 155 km in diameter with 90% credibility. The rotationally averaged occultation based diameter $D_{eq} = 545 \pm 24$ km and derived beaming parameter $\eta = 1.87^{+0.10}_{-0.12}$ are consistent with the values of the thermal analysis reported in Mommert et al. (2012) of $D_{eq} = 523.0^{+35.1}_{-34.4}$ km, $\eta = 1.57^{+0.30}_{-0.23}$ within the uncertainties.

6.9. (28978) Ixion

For Ixion, no satellite is needed to reconcile the occultation and thermal measurements, since the marginalised posterior in d_{eq} peaks at 0. Lellouch et al. (2013) report a fit of the single body NEATM model with $D_{\text{eq}} = 617^{+19}_{-20}$ km and $\eta = 0.91^{+0.04}_{-0.06}$. The area-equivalent diameter measured with occultations of $D_{\text{eq}} = 697 \pm 10$ km is considerably larger. Therefore, we infer a beaming parameter of $\eta = 1.11^{+0.04}_{-0.06}$, larger than Lellouch et al. (2013), as an increasing beaming parameter implies a colder temperature distribution (see Eqs. 1 and 2), and consequently diminished thermal emission.

6.10. (470316) 2007 OC10

For 470316 we find a 90% credibility upper limit on the area-equivalent diameter for a putative satellite of 218 km. As was the case for Varda, the limited wavelength coverage of the thermal emission combined with a large $\sim 15\%$ relative errorbar in the occultation derived value of D_{eq} , prevents us from setting tighter constraints.

Our results are almost identical to those of Gómez-Limón et al. (2025) (see their Figure 6), where the reported 90% credibility upper limit on d_{eq} is 225.3 km. The only difference in approaches is that we incorporate the uncertainties in H_V , whereas in Gómez-Limón et al. (2025) the absolute magnitude is fixed to the nominal value of $H_V = 5.4$.

As was the case for 84922, the occultation based diameter $D_{\text{eq}} = 330^{+56}_{-55}$ km and our estimated beaming parameter of $\eta = 1.59^{+0.48}_{-0.61}$ are compatible within 1σ those fitted in Lellouch et al. (2013) with a single-object NEATM: $D_{\text{eq}} = 306^{+93}_{-72}$ km, $\eta = 1.17^{+1.11}_{-0.64}$.

6.11. General results

Our analysis confirms an expected negative correlation between d_{eq} and D_{eq} , physically representing the trade-off required to maintain a constant integrated thermal flux. For objects where a satellite is inferred, ordinary least squares regression yields steep slopes between -1.5 and -2.0 (with Achlys reaching a marked -3.9). In contrast, targets compatible with a single-body model exhibit a much weaker dependence, with slopes ranging only from -0.1 to -0.7 . This inverse relationship dictates that as the primary's size decreases, the secondary's size must increase to account for the total observed flux.

Because of this correlation, results for objects with large rotational variability (leading to uncertain D_{eq} values) should be taken with caution, especially d_{eq} estimates when a satellite is inferred. However, for our sample of TNOs we have small amplitudes for their rotational light curves, see Table 1. This is an indication that the projected area should not vary much along rotation. For reference, assuming that the reflected flux is directly proportional to the projected area, a light curve amplitude of 0.1 mag translates to $\sim 5\%$ rotational variability in projected area-equivalent diameter.

The only object with a notably high rotational light curve amplitude is 84922. For this TNO we have used as input value for D_{eq} the mean equivalent diameter estimated in Vara-Lubiano et al. (2022) by combining the projected area in the occultation with the known rotational phase at the occultation instant. This choice should mitigate the impact that rotational effects might cause on our inference on the value of d_{eq} .

From the pairwise plots available in Figures 2 and 3, we can see that the free parameter d_{eq} and the absolute magnitude are uncorrelated. This is reflected in the fact that the results presented here for 470316 are virtually the same as those exposed in Gómez-Limón et al. (2025), where uncertainties in H_V were not considered.

7. Conclusions

In this paper, we have developed and implemented a Bayesian framework to constrain the presence of unresolved satellites around Trans-Neptunian Objects, independent of primary-to-secondary separation. By combining radiometric thermal data with high-precision size measurements from stellar occultations, we provide a systematic approach that advances the field beyond previous qualitative or non-uniform analyses. Our methodology exploits the discrepancy between the area-equivalent diameters derived from occultations and the larger effective diameters often inferred from single-object thermal models. By rigorously modelling the observed thermal fluxes with a binary object model, we are able to indirectly detect companions and constrain their sizes in a way that is both reproducible and scalable to larger TNO populations. The main conclusions of this study can be summarised as follows:

- For three out of the four targets with known satellites, we recover the presence of a companion. For the case of the target with the smallest satellite, G!kún||hòmdímà we report an upper limit for d_{eq} consistent with the estimated size of its satellite G!ò'é!hú. Therefore, our methodology delivers coherent results for these validation targets.

In the case of Achlys, the reported satellite size is larger than expected from the measured difference in brightness between primary and secondary. This could be due to a $\sim 5\%$ underestimation of D_{eq} from occultation data. The results could also possibly be reconciled if this difference in brightness constraint is imposed and an extra degree of freedom is added to the model, allowing the primary and secondary to have different albedos. Another possibility is to model Achlys as a triple system. However, this is beyond the scope of the present paper.

For Huya and Varda, our estimated satellite sizes are compatible with the estimates available in the literature. This is especially encouraging for the case of Huya, which has complete thermal emission wavelength coverage within "TNOs are Cool", a very accurate measurement of D_{eq} , and a reliable constraint on the real value of d_{eq} from stellar occultations.

- We find that for four objects (including G!kún||hòmdímà), no satellite is needed to reconcile thermal and occultation observations, and we provide upper limits on the size of any putative companion. For the other six objects, we find that the presence of a satellite provides a better explanation of the measured fluxes from "TNOs are Cool", taking into account the observed occultation sizes.

This corresponds to a nominal binarity fraction of 60% within our sample. However, we emphasize that this value is derived from a small ($N = 10$) and heterogeneous set of objects, and is therefore not directly comparable to population-level estimates. For reference, Porter et al. (2024) report a binary fraction of 21.2% based on a much larger ($N = 198$) and homogeneous sample of Cold Classical TNOs observed with HST.

- Our analysis provides compelling evidence that (307261) Máni, (84522) 2002 TC302, and (119951) 2002 KX14 are

Table 2: Summary of our results.

Object	Satellite inferred	Known satellite	Observed d_{eq} (km)	Inferred d_{eq} (km)	Inferred p_V	Inferred η
(208996) Achlys	Yes	Yes	77^{+10}_{-11}	236^{+64}_{-52}	$0.083^{+0.009}_{-0.009}$	$1.18^{+0.04}_{-0.04}$
(229762) G!kún 'hòmdímà	No	Yes	$139.5^{+2.9}_{-2.9}$	<159.1	$0.146^{+0.017}_{-0.017}$	$1.43^{+0.13}_{-0.18}$
(38628) Huya	Yes	Yes	> 165*	217^{+25}_{-22}	$0.079^{+0.004}_{-0.004}$	$0.98^{+0.03}_{-0.03}$
(174567) Varda	Yes	Yes	$332.9^{+9.1}_{-8.8}$	332^{+184}_{-158}	$0.097^{+0.017}_{-0.014}$	$0.91^{+0.14}_{-0.20}$
(84522) 2002 TC302	Yes	No	-	272^{+114}_{-92}	$0.111^{+0.019}_{-0.022}$	$1.11^{+0.12}_{-0.16}$
(119951) 2002 KX14	Yes	No	-	251^{+65}_{-57}	$0.084^{+0.011}_{-0.013}$	$1.85^{+0.16}_{-0.21}$
(307261) Máni	Yes	No	-	534^{+58}_{-54}	$0.068^{+0.004}_{-0.005}$	$1.12^{+0.03}_{-0.04}$
(84922) 2003 VS2	No	No	-	<96.9	$0.128^{+0.010}_{-0.011}$	$1.87^{+0.10}_{-0.12}$
(28978) Ixion	No	No	-	<62.3	$0.104^{+0.003}_{-0.003}$	$1.11^{+0.04}_{-0.05}$
(470316) 2007 OC10	No	No	-	<131.2	$0.100^{+0.017}_{-0.036}$	$1.59^{+0.48}_{-0.61}$

Notes. A target is marked as "Satellite inferred" if the posterior in d_{eq} peaks at a non-zero value. For details see Section 5. When an upper limit is reported, it corresponds to 68 % credibility. For our validation targets (except Huya), the reported literature d_{eq} value is computed from the observed magnitude difference (see Section 3) and the measured D_{eq} from occultations (see Table 1), under the assumption of equal albedos for both components. * For Huya, the literature lower limit comes from a direct detection from a stellar occultation (Rommel et al. 2025).

TNBs. For these targets, the size constraints from multi-chord occultations are very reliable thanks to great observational coverage and low expected rotational variability. We infer significant sizes for the putative satellites of these targets, with primary-to-secondary diameter ratios ranging from 3:2 to 2:1. These ratios represent an intermediate regime between the near-equal-sized binaries typically produced via Streaming Instability models and the high-mass-ratio systems composed of large TNOs with smaller moons. However, these size ratio estimates must be taken with care as they come from our assumption of equal surface properties.

These objects have been targeted by both HST imaging and stellar occultations, but no companions have been reported to date. However, several geometric configurations and small angular separations could explain why such satellites remained undetected in previous observations. Further observations are essential to confirm these findings. Stellar occultations with broad spatial coverage represent the most promising technique for this purpose.

- In Appendix A, we quantitatively assessed the impact of non-spherical geometries and different emissivity values on our results. Our analysis demonstrates that the observed excess thermal flux in the targets for which we infer the presence of a satellite cannot be explained with values of the emissivity different from $\epsilon = 0.9$. Crucially, we also prove that the spherical approximation within the NEATM does not introduce a systematic bias toward smaller fluxes, leading to an overestimation of satellite sizes. Instead, plausible ellipsoidal models yield a scatter of flux values around the spherical prediction. While this increases the variance, it does not result in a shift that would lead to systematic false-positive satellite detections. We acknowledge that for 119951 and 84522, certain triaxial geometries could potentially account for the observed thermal emission. However, fully constraining a triaxial shape-spin model involves a significantly larger parameter space and a level of complexity that remains outside the scope of this work. At present, the available occultation data for these targets are insufficient to faithfully

constrain the numerous degrees of freedom of such a triaxial spin-shape model. Nevertheless, our current statistical framework suggests that, under the assumption of random pole orientations, the observed flux excesses are likely not due to departures from sphericity.

Rotational variability could be an influential factor for targets with shapes departing considerably from sphericity. For the cases of Achlys and 84922, we addressed this issue by using rotationally averaged D_{eq} values. For the rest of targets, rotational variability is expected to be very low from their light curve amplitudes.

- The thermal wavelength coverage is very influential in the accuracy of the results from our methodology. The uncertainties obtained for targets with only *Herschel*/PACS data are significantly larger than for those with also *Spitzer*/MIPS and *Herschel*/SPIRE data. Varda and Huya represent a clear example: Both objects show $\sim 2\%$ relative uncertainty in the occultation-derived diameter (see Table 1). For Varda, whose thermal emission was only covered by *Herschel*/PACS, the obtained relative uncertainty in d_{eq} is $\sim 50\%$ and in η it is $\sim 20\%$. Conversely, Huya was also observed with *Spitzer*/MIPS, *Herschel*/SPIRE and ALMA, and shows relative uncertainties of $\sim 10\%$ and $\sim 3\%$ in d_{eq} and η respectively.
- Recent work by Lyra (2025) highlighted a "dearth" of trans-Neptunian binaries between absolute magnitudes 4 and 5. While many individual TNOs occupy this range, the lack of known binaries suggests either primordial disruption or an observational bias toward undetected companions. Distinguishing between these scenarios is critical. If the gap is physical, Lyra (2025) propose a hypothesis where pebble accretion stripped primordial companions for the planetesimals closest to the sun, while driving their growth. These objects will result in the current high-mass TNBs, whose satellites should be products of recent collisions. In contrast, smaller objects that did not undergo significant pebble accretion resulted in the currently known smaller TNBs, which are primordial.

The low mass-limit edge of the gap seems to be consistent with the high-end mass of the size distribution of Cold Classical TNOs (Kavelaars et al. 2021), a dynamical class where

many equal-sized binaries are present. The high-mass end is of uncertain origin, with binaries above this edge being mainly hot classicals, scattered disk or resonant objects with smaller satellites in tight orbits. There are only two currently known TNBs in the $4 < H < 5$ range: (120347) Salacia (scattered disk object) and (82075) 2000 YW134 (resonant object). They share characteristics with the population of larger TNBs, being the primary-to-secondary diameter ratio roughly 3:1 for both and a separation on the order of 10^{-3} Hill radii (see Johnston (2019) and references therein).

With our methodology, we find that (84522) 2002 TC302 and (119951) 2002 KX14 are likely binary systems, and they are both in the 4th to 5th absolute magnitude range, see Figure 1. 84522 is a resonant TNO, whereas 119951 is a classical TNO with very low inclination (Rizos et al. 2025), that could be classified as cold classical although it might also be part of the low-inclination tail of the hot population (Fernández-Valenzuela et al. 2021). The inferred size ratios and potentially tight orbit (consistent with no-detection from HST imaging) indicate that these systems also follow the trend of TNBs above the high-mass end of the gap.

Confirmation of these putative satellites would double the known TNB population within this magnitude range, suggesting the gap is an artifact of observational bias rather than physical disruption. This would challenge the hypothesis that massive TNBs with small companions are exclusively products of recent collisions, favouring instead a scenario where TNOs retain primitive satellites which are below current detection thresholds.

- Beyond the shape constraints previously discussed, the NEATM framework may be inherently limited for certain targets due to unmodeled physical processes. The presence of undetected ring systems, for instance, could contribute significant thermal emission that is not captured by standard single or binary models (Lellouch et al. 2017; Müller et al. 2019; Kiss et al. 2024b). Furthermore, while less probable, the thermal energy balance of some objects could be perturbed by the sublimation of surface ices or active cryovolcanism (Kiss et al. 2024a). The fact that neither the single-body models in existing literature nor the binary configurations proposed in this work perfectly reproduce the full multi-wavelength spectral energy distribution for every target suggests that simplified thermal approximations have reached their predictive limit. These remaining discrepancies likely reflect a combination of complex surface physics and the inherent systematic uncertainties associated with the reduction and calibration of low-signal-to-noise thermal data.
- Finally, this work highlights the critical importance of obtaining multi-chord stellar occultations for targets of the "TNOs are Cool" survey, especially if they have broad thermal wavelength coverage. The synergy between occultation-derived diameters and radiometric data significantly enhances the scientific value of the legacy measurements provided by *Herschel* and *Spitzer*. It is important to emphasise that sensitive photometric observations at $\sim 100 \mu\text{m}$, where the thermal emission of TNOs typically peaks, will remain unavailable for the near future, as no current space-borne or ground-based facilities cover this spectral range. Consequently, it is essential to maximise the scientific return of the existing "TNOs are Cool" dataset with approaches such as the one presented here.

knowledge Flavia Luane Rommel for her insights on Máni. We acknowledge the use of the publicly available Python wrapper for NEATM modelling developed by Michael Müller. The authors of IAA-CSIC acknowledge financial support from the Severo Ochoa grant CEX2021-001131-S funded by MCIN/AEI/ 10.13039/501100011033. This work was partially funded by the Spanish projects PID2020-112789GB-I00 (AEI) and Proyecto de Excelencia de la Junta de Andalucía PY20-01309. P.S.-S. and Y.K. acknowledge financial support from the Spanish I+D+i project PID2022-139555NB-I00 (TNO-JWST) funded by MCIN/AEI/10.13039/501100011033. This research has made use of LTE's SsODNet VO service (<https://ssp.imcce.fr/webservices/ssodnet/>).

References

- Alvarez-Candal, A., Pinilla-Alonso, N., Ortiz, J. L., et al. 2016, *Astronomy & Astrophysics*, 586, A155
- Bai, X.-N. & Stone, J. M. 2010, *The Astrophysical Journal*, 722, 1437
- Belskaya, I. N., Levasseur-Regourd, A.-C., Shkuratov, Y. G., & Muinonen, K. 2008, in *The Solar System Beyond Neptune*, ed. M. A. Barucci, H. Boehnhardt, D. P. Cruikshank, A. Morbidelli, & R. Dotson (University of Arizona Press), 115–127
- Benedetti-Rossi, G., Santos-Sanz, P., Ortiz, J. L., et al. 2019, *The Astronomical Journal*, 158, 159
- Benedetti-Rossi, G., Sicardy, B., Buie, M. W., et al. 2016, *The Astronomical Journal*, 152, 156
- Bessell, M., Castelli, F., & Plez, B. 1998, *Astronomy & Astrophysics*, 333, 231
- Binzel, R. P., Gehrels, T., & Matthews, M. S. 1989, *Asteroids II*
- Brown, M. & Suer, T.-A. 2007, *International Astronomical Union Circular*, 8812, 1
- Brucker, M., Grundy, W., Stansberry, J., et al. 2009, *Icarus*, 201, 284
- Canup, R. M. 2005, *Science*, 307, 546
- Carrera, D., Gorti, U., Johansen, A., & Davies, M. B. 2017, *The Astrophysical Journal*, 839, 16
- Christy, J. W. & Harrington, R. S. 1978, *Astronomical Journal*, vol. 83, Aug. 1978, p. 1005, 1007, 1008., 83, 1005
- Delbo, M., dell'Oro, A., Harris, A. W., Mottola, S., & Mueller, M. 2007, *Icarus*, 190, 236
- Denton, C. A., Asphaug, E., Emsenhuber, A., & Melikyan, R. 2025, *Nature Geoscience*, 18, 37
- Dias-Oliveira, A., Sicardy, B., Ortiz, J., et al. 2017, *The Astronomical Journal*, 154, 22
- Farkas-Takács, A., Kiss, C., Vilenius, E., et al. 2020, *Astronomy & Astrophysics*, 638, A23
- Fernández, J. A. 2020, in *The Trans-Neptunian Solar System* (Elsevier), 1–22
- Fernández-Valenzuela, E., Pinilla-Alonso, N., Stansberry, J., et al. 2021, *The Planetary Science Journal*, 2, 10
- Foreman-Mackey, D., Hogg, D. W., Lang, D., & Goodman, J. 2013, *Publications of the Astronomical Society of the Pacific*, 125, 306
- Fornasier, S., Lellouch, E., Müller, T., et al. 2013, *Astronomy & Astrophysics*, 555, A15
- Fraser, W. C., Bannister, M. T., Pike, R. E., et al. 2017, *Nature Astronomy*, 1, 1
- Fraser, W. C., Batygin, K., Brown, M. E., & Bouchez, A. 2013, *Icarus*, 222, 357
- Gelman, A., Carlin, J. B., Stern, H. S., et al. 2013, *Bayesian data analysis, Third Edition* (Chapman and Hall/CRC)
- Gladman, B. & Volk, K. 2021, *Annual Review of Astronomy and Astrophysics*, 59, 203
- Gómez-Limón, J. M., Leiva, R., Ortiz, J., et al. 2025, *Astronomy & Astrophysics*, 697, A157
- Goodman, J. & Weare, J. 2010, *Commun. Appl. Math. Comput. Sci.*, 5, 65
- Gregory, P. 2005, *Bayesian logical data analysis for the physical sciences: A comparative approach with Mathematica® support* (Cambridge University Press)
- Grundy, W. M., Noll, K. S., Buie, M. W., et al. 2019a, *Icarus*, 334, 30
- Grundy, W. M., Noll, K. S., Nimmo, F., et al. 2011, *Icarus*, 213, 678
- Grundy, W. M., Noll, K. S., Roe, H. G., et al. 2019b, *Icarus*, 334, 62
- Grundy, W. M., Porter, S. B., Benecchi, S. D., et al. 2015, *Icarus*, 257, 130
- Harris, A. W. 1998, *Icarus*, 131, 291
- Holler, B. J., Grundy, W. M., Buie, M. W., & Noll, K. S. 2021, *Icarus*, 355, 114130
- Hovis Jr, W. & Callahan, W. R. 1966, *Journal of the Optical Society of America*, 56, 639
- Johansen, A., Oishi, J. S., Low, M.-M. M., et al. 2007, *Nature*, 448, 1022
- Johnston, W. 2019, *NASA Planetary Data System*, 4
- Kavelaars, J., Petit, J.-M., Gladman, B., et al. 2021, *The Astrophysical journal letters*, 920, L28
- Kilic, Y., Braga-Ribas, F., Pereira, C., et al. 2026, *Astronomy & Astrophysics*, 707, A70

Acknowledgements. The authors thank the referee and the editor for their valuable feedback. This publication is funded by the Spanish Ministry of Universities through the university training programme FPU2022/00492. We ac-

- Kiss, C., Marton, G., Farkas-Takács, A., et al. 2017, *The Astrophysical Journal Letters*, 838, L1
- Kiss, C., Müller, T. G., Vilenius, E., et al. 2014, *Experimental Astronomy*, 37, 161
- Kiss, C., Müller, T. G., Farkas-Takács, A., et al. 2024a, *The Astrophysical Journal Letters*, 976, L9
- Kiss, C., Müller, T. G., Marton, G., et al. 2024b, *Astronomy & Astrophysics*, 684, A50
- Kretlow, M., Ortiz, J., Desmars, J., et al. 2024, *Astronomy & Astrophysics*, 691, A31
- Leinhardt, Z. M., Marcus, R. A., & Stewart, S. T. 2010, *The Astrophysical Journal*, 714, 1789
- Lellouch, E., Moreno, R., Müller, T., et al. 2017, *Astronomy & Astrophysics*, 608, A45
- Lellouch, E., Santos-Sanz, P., Lacerda, P., et al. 2013, *Astronomy & Astrophysics*, 557, A60
- Lim, T. L., Stansberry, J., Müller, T. G., et al. 2010, *Astronomy & Astrophysics*, 518, L148
- Lyra, W. 2025, *Icarus*, 442, 116737
- Mommert, M., Harris, A. W., Kiss, C., et al. 2012, *Astronomy & Astrophysics*, 541, A93
- Morgado, B. E., Sicardy, B., Braga-Ribas, F., et al. 2023, *Nature*, 614, 239
- Müller, T., Kiss, C., Ali-Lagoa, V., et al. 2019, *Icarus*, 334, 39
- Müller, T. G., Lellouch, E., Bönhardt, H., et al. 2009, *Earth, Moon, and Planets*, 105, 209
- Müller, T., Lellouch, E., & Fornasier, S. 2020, in *The Trans-Neptunian Solar System*, ed. D. Prrialnik, M. A. Barucci, & L. A. Young (Elsevier), 153–181
- Nesvorný, D. 2018, *Annual Review of Astronomy and Astrophysics*, 56, 137
- Nesvorný, D., Li, R., Youdin, A. N., Simon, J. B., & Grundy, W. M. 2019, *Nature Astronomy*, 3, 808
- Nesvorný, D. & Vokrouhlický, D. 2019, *Icarus*, 331, 49
- Nesvorný, D., Youdin, A. N., & Richardson, D. C. 2010, *The Astronomical Journal*, 140, 785
- Noll, K., Grundy, W., Schlichting, H., Murray-Clay, R., & Benecchi, S. 2012, *International Astronomical Union Circular*, 9253, 2
- Noll, K. S., Grundy, W. M., Nesvorný, D., & Thirouin, A. 2020, in *The Trans-Neptunian Solar System*, ed. D. Prrialnik, M. A. Barucci, & L. A. Young (Elsevier), 205–224
- Ortiz, J., Gutiérrez, P., Casanova, V., & Sota, A. 2003, *Astronomy & Astrophysics*, 407, 1149
- Ortiz, J., Gutiérrez, P., Santos-Sanz, P., Casanova, V., & Sota, A. 2006, *Astronomy & Astrophysics*, 447, 1131
- Ortiz, J., Thirouin, A., Campo Bagatin, A., et al. 2012, *Monthly Notices of the Royal Astronomical Society*, 419, 2315
- Ortiz, J. L. 2020, *Thermal diameters versus occultation diameters of TNOs: a new tool to search for satellites?*, Tech. rep., Copernicus Meetings
- Ortiz, J. L., Santos-Sanz, P., Sicardy, B., et al. 2017, *Nature*, 550, 219
- Ortiz, J. L., Santos-Sanz, P., Sicardy, B., et al. 2020a, *Astronomy & Astrophysics*, 639, A134
- Ortiz, J. L., Sicardy, B., Camargo, J. I., Santos-Sanz, P., & Braga-Ribas, F. 2020b, in *The trans-neptunian solar system* (Elsevier), 413–437
- Parker, A. H., Buie, M. W., Grundy, W. M., & Noll, K. S. 2016, *The Astrophysical Journal Letters*, 825, L9
- Parker, A. H., Kavelaars, J. J., Petit, J.-M., et al. 2011, *The Astrophysical Journal*, 743, 1
- Perna, D., Barucci, M. A., Fornasier, S., et al. 2010, *Astronomy & Astrophysics*, 510, A53
- Perna, D., Dotto, E., Barucci, M., et al. 2013, *Astronomy & Astrophysics*, 554, A49
- Poglitsch, A., Waelkens, C., Geis, N., et al. 2010, *Astronomy & Astrophysics*, 518, L2
- Porter, S. B., Benecchi, S. D., Verbiscer, A. J., et al. 2024, *The Planetary Science Journal*, 5, 143
- Porter, S. B. & Grundy, W. M. 2012, *Icarus*, 220, 947
- Ragozzine, D. & Brown, M. E. 2009, *The Astronomical Journal*, 137, 4766
- Rieke, G., Young, E., Engelbracht, C., et al. 2004, *The Astrophysical Journal Supplement Series*, 154, 25
- Rizos, J., Ortiz, J., Rommel, F., et al. 2025, *Astronomy & Astrophysics*, 697, A62
- Robert, C. P. 2007, *The Bayesian choice: from decision-theoretic foundations to computational implementation* (Springer)
- Rommel, F., Fernández-Valenzuela, E., Proudfoot, B., et al. 2025, *The Planetary Science Journal*, 6, 48
- Rommel, F. L., Braga-Ribas, F., Ortiz, J., et al. 2023, *Astronomy & Astrophysics*, 678, A167
- Santos-Sanz, P., Lellouch, E., Fornasier, S., et al. 2012, *Astronomy & Astrophysics*, 541, A92
- Santos-Sanz, P., Lellouch, E., Groussin, O., et al. 2017, *Astronomy & Astrophysics*, 604, A95
- Santos-Sanz, P., Ortiz, J. L., Sicardy, B., et al. 2022, *Astronomy & Astrophysics*, 664, A130
- Schindler, K., Wolf, J., Bardecker, J., et al. 2017, *Astronomy & Astrophysics*, 600, A12
- Sheppard, S. S. 2007, *The Astronomical Journal*, 134, 787
- Sicardy, B., Ortiz, J., Assafin, M., et al. 2011, *Nature*, 478, 493
- Sickafoose, A., Bosh, A., Levine, S., et al. 2019, *Icarus*, 319, 657
- Souami, D., Braga-Ribas, F., Sicardy, B., et al. 2020, *Astronomy & Astrophysics*, 643, A125
- Stansberry, J., Grundy, W., Mueller, M., et al. 2012, *Icarus*, 219, 676
- Tegler, S. C., Romanishin, W., & GJ Consolmagno, S. 2016, *The Astronomical Journal*, 152, 210
- Thirouin, A. 2013, doctoral thesis, Universidad de Granada
- Thirouin, A., Noll, K. S., Ortiz, J., & Morales, N. 2014, *Astronomy & Astrophysics*, 569, A3
- Thirouin, A., Ortiz, J., Duffard, R., et al. 2010, *Astronomy & Astrophysics*, 522, A93
- Thuillier, G., Floyd, L., Woods, T., et al. 2004, *Advances in Space Research*, 34, 256
- Vara-Lubiano, M., Benedetti-Rossi, G., Santos-Sanz, P., et al. 2022, *Astronomy & Astrophysics*, 663, A121
- Veillet, C., Parker, J. W., Griffin, I., et al. 2002, *Nature*, 416, 711
- Verbiscer, A. J., Helfenstein, P., Porter, S. B., et al. 2022, *The Planetary Science Journal*, 3, 95
- Vilenius, E., Kiss, C., Mommert, M., et al. 2012, *Astronomy & Astrophysics*, 541, A94
- Vilenius, E., Kiss, C., Müller, T., et al. 2014, *Astronomy & Astrophysics*, 564, A35
- Volk, K. & Van Laerhoven, C. 2024, *Research Notes of the AAS*, 8, 36
- Weaver, H., Buie, M., Buratti, B., et al. 2016, *Science*, 351, aae0030
- Weaver, H. A., Stern, S., Mutchler, M., et al. 2006, *Nature*, 439, 943
- Youdin, A. N. & Goodman, J. 2005, *The Astrophysical Journal*, 620, 459

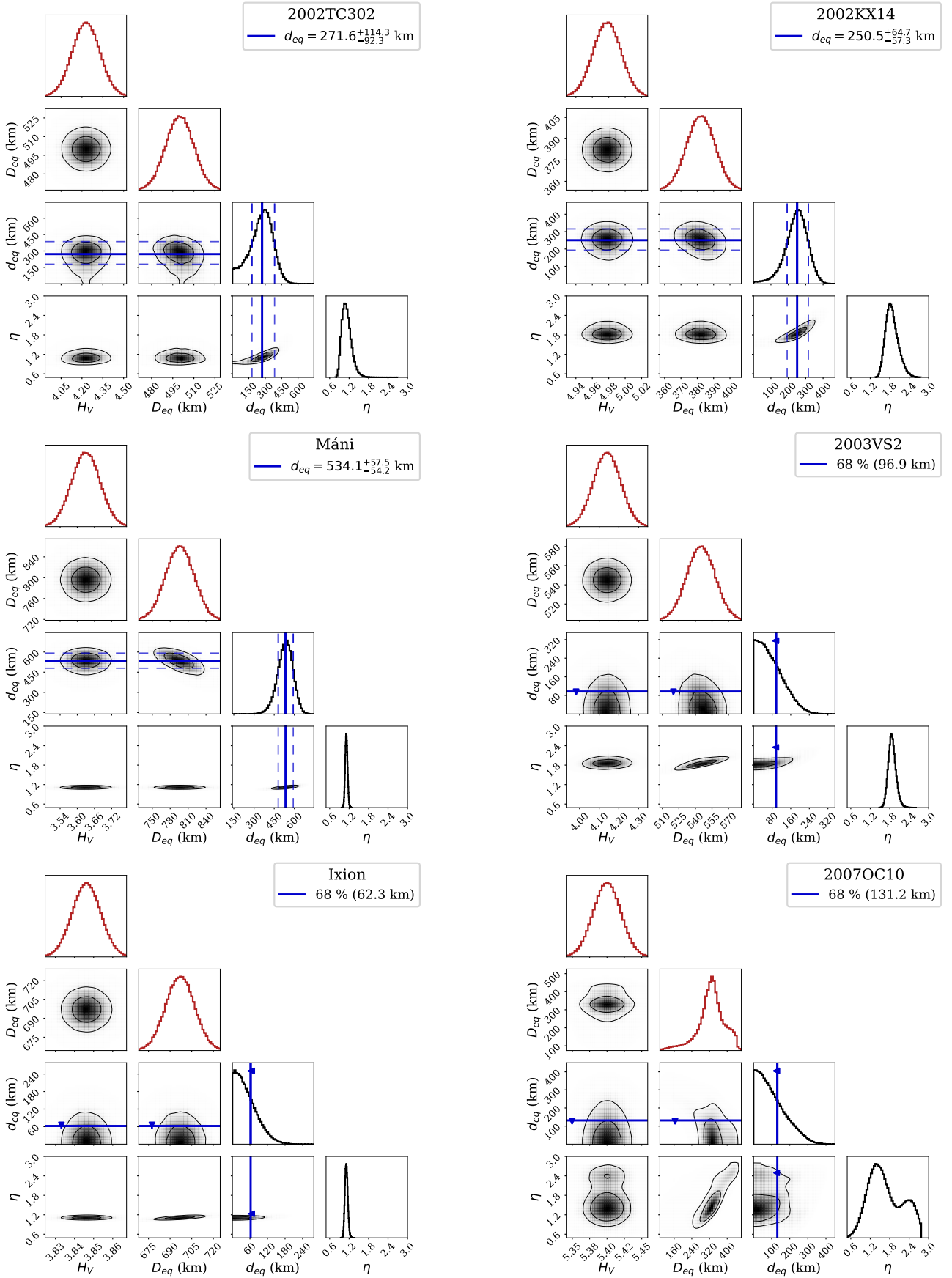


Fig. 3: Pairwise plots for non-validation targets. The marginalised posterior pdfs of H_V and D_{eq} are shown in red to highlight the fact that these are not free parameters. These pdfs represent the independent measurements of H_V and D_{eq} from literature, reported in Table 1, that were included in the analysis.

Appendix A: Robustness analysis with respect to model assumptions

A.1. Effects of emissivity

Emissivity is a measure of a material's surface efficiency in emitting thermal radiation compared to a perfect blackbody. By definition, it is bounded in the $[0, 1]$ range. The choice of an emissivity $\epsilon = 0.9$ for the "TNOs are Cool" works is based on laboratory measurements of silicate powder (Hovis Jr & Callahan 1966), which is thought to resemble the properties of small Solar System bodies (Vilenius et al. 2012). It is reasonable to question whether a different value of ϵ might explain the discrepant occultation and thermal measurements without the need to invoke a satellite. To test this possibility, we take 119951 as an example. In Figure A.1 we plot the spectral energy distribution (SED) of 119951 simulated under the NEATM considering a single body with the observed absolute magnitude and area-equivalent diameter. For a reasonable choice of $\eta = 1.8$ (see Figure 3 and Vilenius et al. (2012)), we considered the standard emissivity $\epsilon = 0.9$, a high emissivity of $\epsilon = 0.98$ typical of water ice, and a very damped emissivity of $\epsilon = 0.5$. None of these choices can explain the flux values observed in the thermal measurements. We conclude that the observed thermal excesses are not attributable to emissivity values different from $\epsilon = 0.9$.

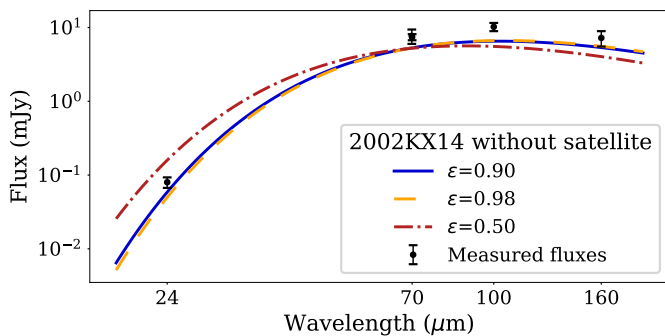


Fig. A.1: (119951) 2002 KX14 thermal SED simulations assuming no satellite and different emissivities. We considered the D_{eq} and H_V values in Table 1 and $\eta = 1.8$. No value of ϵ delivers a good fit to the data.

A.2. Effects of non-spherical shapes

While the standard NEATM assumes a spherical shape, the observed occultation projections of our targets indicate significant oblateness. It is therefore necessary to test whether accounting for non-spherical geometries could resolve the inconsistencies between the thermal and occultation data, thereby rendering the unresolved satellite hypothesis unnecessary.

We performed simulations with a thermal model identical to the NEATM, but assuming an ellipsoidal shape with semi-axes $a \geq b \geq c$, where the minor axis is coincident with the spin axis. These simulations are performed for the objects for which we infer the presence of previously undetected satellites: (84522) 2002 TC302, (119951) 2002 KX14, and (307261) Máni. For each object we considered the η value fitted within the NEATM in the "TNOs are Cool" papers (Vilenius et al. 2012; Fornasier et al. 2013). We considered only ellipsoids compatible with the observed light curve amplitudes and projected elliptical limbs (with semi-axes a', b') in occultations. To take this into account,

Table A.1: Simulated-to-measured flux ratios for single-object ellipsoidal models.

Object	24 μm	71 μm	70 μm	100 μm	160 μm
84522	$0.79^{+0.09}_{-0.16}$	-	$0.89^{+0.07}_{-0.11}$	$0.59^{+0.04}_{-0.06}$	$1.27^{+0.08}_{-0.13}$
119951	$0.69^{+0.07}_{-0.29}$	$0.70^{+0.09}_{-0.21}$	$0.72^{+0.09}_{-0.21}$	$0.65^{+0.08}_{-0.17}$	$0.76^{+0.13}_{-0.15}$
Máni	$0.68^{+0.04}_{-0.06}$	$0.78^{+0.03}_{-0.04}$	$0.73^{+0.03}_{-0.04}$	$0.64^{+0.03}_{-0.03}$	$0.83^{+0.03}_{-0.04}$

Notes. We report the mean values across the 1000 accepted models as the nominal values and we compute the 68% highest density intervals to provide errorbars.

we generated random ellipsoids for each object. We chose random spin pole orientations. The semi-axis values are chosen randomly within reasonable bounds. For 119951 and Máni we took into account that a spheroidal shape (where $a = b = a'$) is likely (Rizos et al. 2025; Rommel et al. 2023):

- 84522: $a \in [250, 300]$ km, $b \in [a/2, a]$ km, $c \in [b/2, b]$ km.
- 119951: $a \in [230, 250]$ km, $b \in [0.9a, a]$ km, $c \in [b/2, b]$ km.
- Máni: $a \in [400, 425]$ km, $b \in [0.9a, a]$ km, $c \in [b/2, b]$ km.

We excluded ellipsoidal models whose light curve amplitudes according to (Binzel et al. 1989, Eq. 5, p. 426) were inconsistent with the values in Table 1 within 1σ . Additionally, we discarded models where the projected elliptical limb semi-axes at the occultation epoch deviated by more than 1σ from the fitted values reported in Ortiz et al. (2020a), Rizos et al. (2025) and Rommel et al. (2023) respectively. We repeated the generation of random ellipsoids iteratively until we had 1000 valid models for each object, which are shown in Figure A.2.

For each valid model, we calculated the simulated-to-measured flux ratios (Table A.1). The conclusion is that single-object ellipsoidal models generally tend to underestimate the observed flux. A small subset of models for 84522 and 119951 could reproduce the observations. However, such configurations are statistically improbable under our assumption of random pole orientations.

Crucially, this analysis demonstrates that our methodology is not biased toward satellite detection. Departing from a spherical approximation introduces scatter but does not result in systematically higher fluxes. As shown in Figure A.2, the valid ellipsoidal models yield an ensemble of SEDs centered around the single-body NEATM prediction, confirming that the observed flux excesses cannot be systematically attributed to non-spherical shape effects.

Appendix B: Data-against-model plots

In this appendix section we show multi-panel Figures B.1 and B.2. Each panel corresponds to one target. We plot our modelled SED for the system at thermal wavelengths in a thick black line, for the nominal parameter values shown in the legend, versus the measured thermal fluxes from the "TNOs are Cool" project. Thermal fluxes measured with different instruments are also measured at different epochs and different geometric configurations. We normalize every flux value to the heliocentric distance and target-observer distance from the *Herschel*/PACS observing epoch, which is also the configuration for which the thermal SED is plotted. We also plot 100 randomly selected samples from our posterior MCMC estimates, displayed in thin grey lines, representing the uncertainties in our parameter estimates.

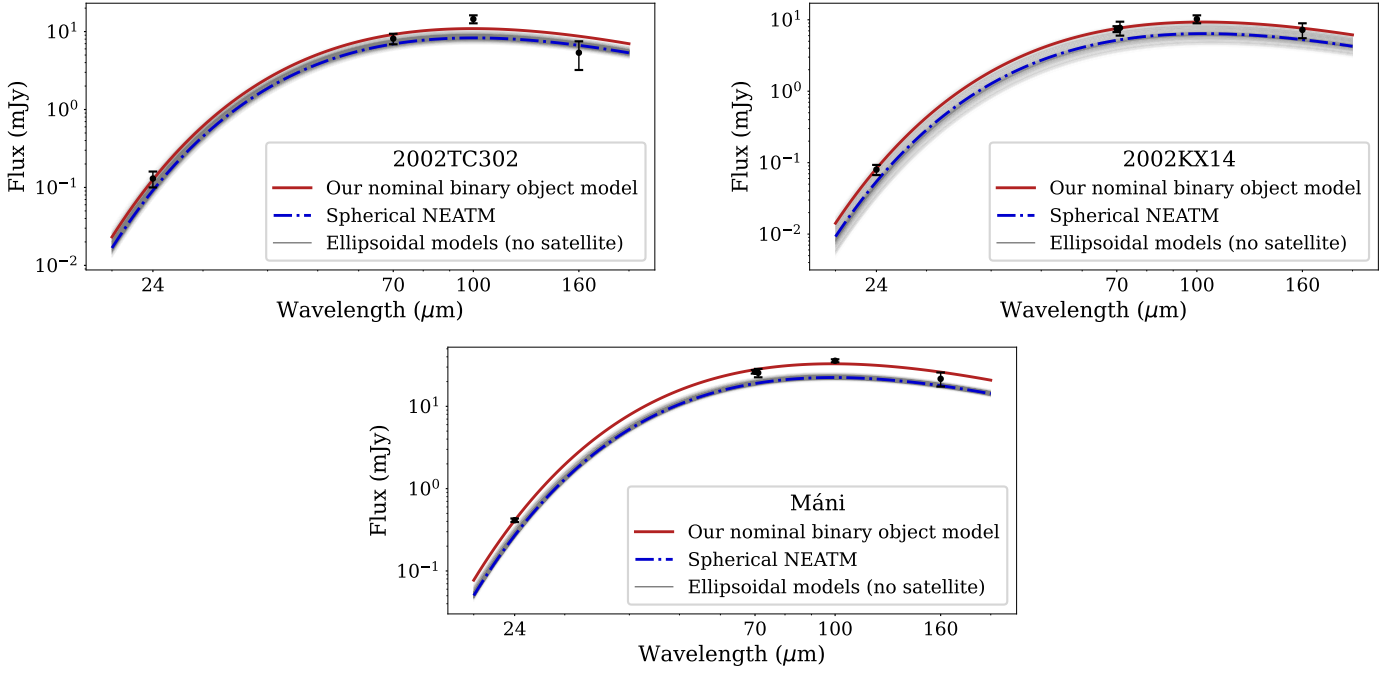


Fig. A.2: Ellipsoidal models vs. our nominal binary object models for the targets for which we infer the presence of a satellite. The SED for the ellipsoidal models tend to underestimate the measured thermal fluxes, while a binary model provides a better fit to the data. The single-object spherical NEATM with the parameters from Table 1 is also plotted for reference.

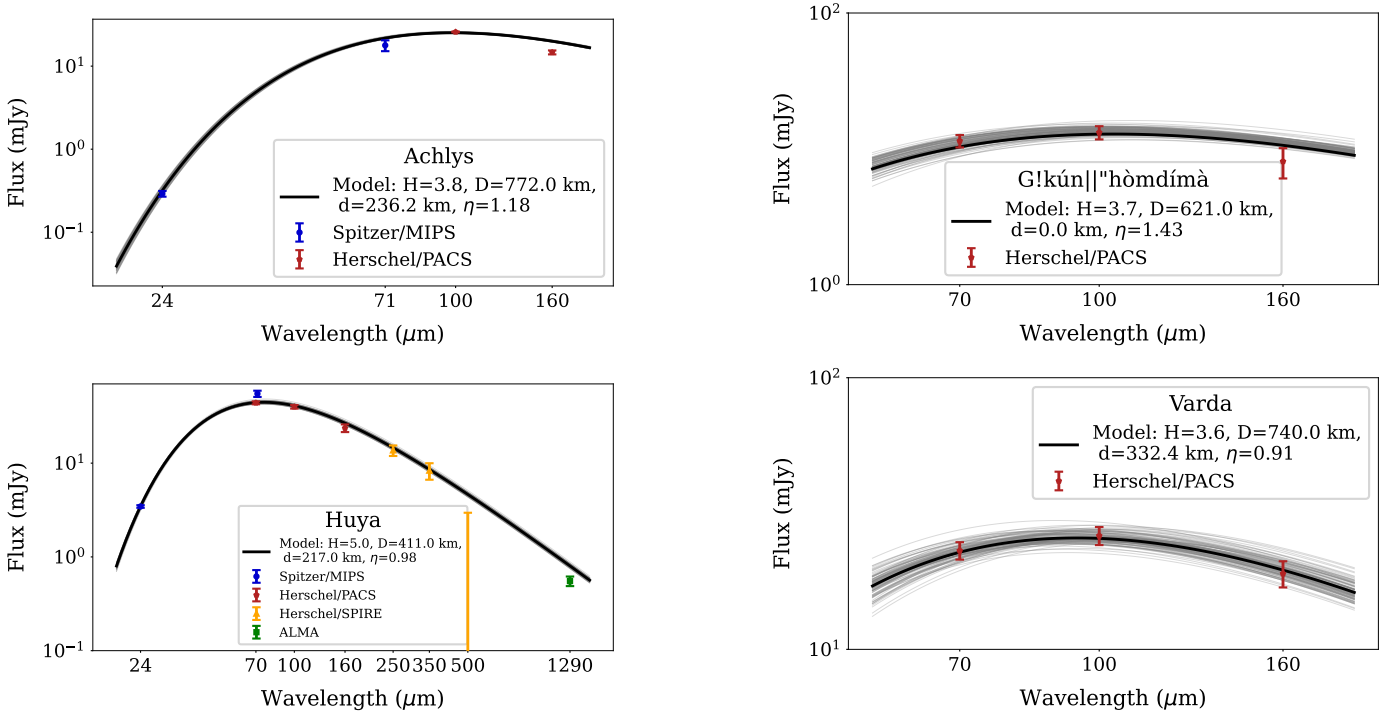


Fig. B.1: Modelled thermal emission for validation targets. See Appendix B for details.

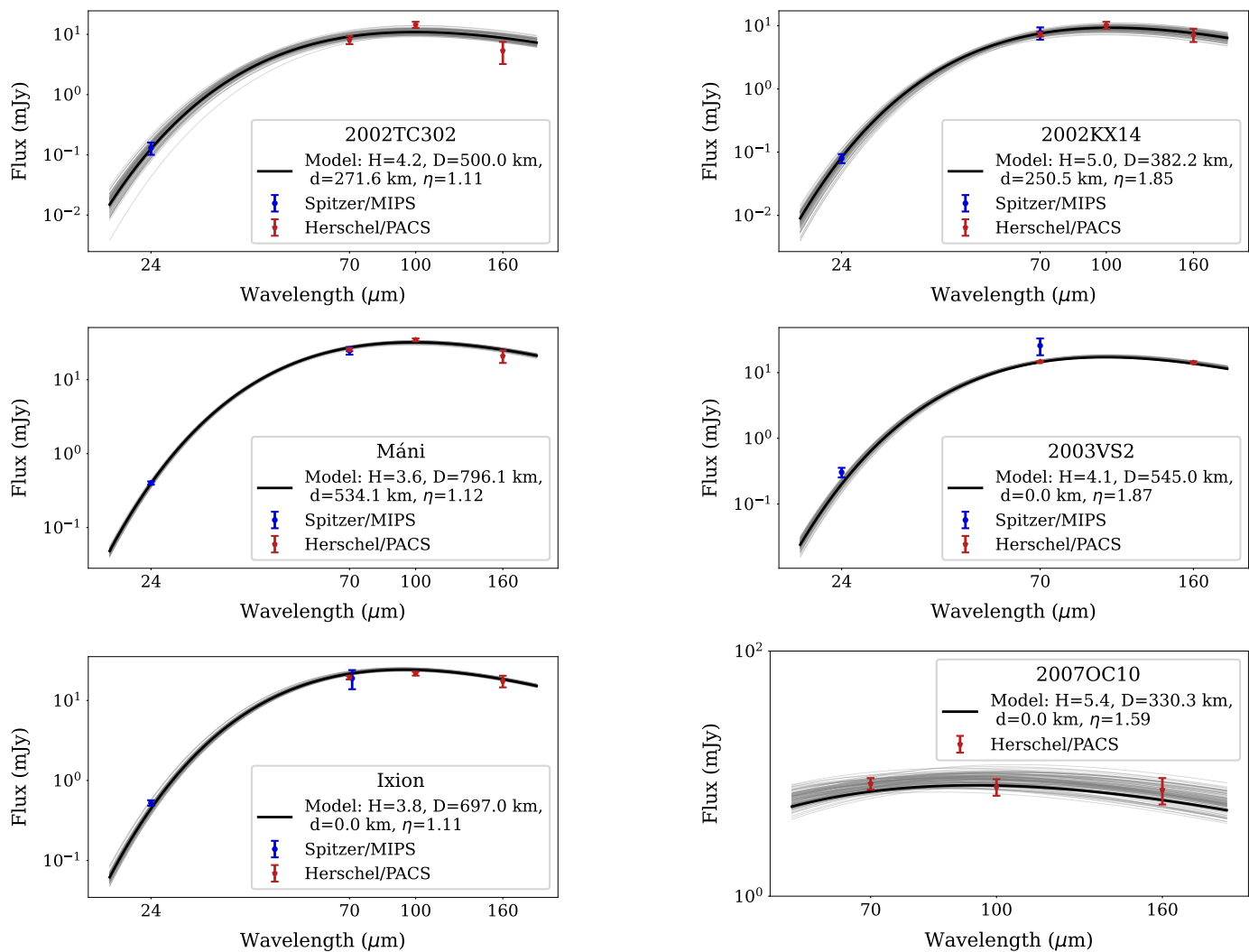


Fig. B.2: Modelled thermal emission for non-validation targets. See Appendix B for details.